First satellite-detected perturbations of outgoing longwave radiation associated with blowing snow events over Antarctica

Yuekui Yang[1,2], Stephen P. Palm[2,3], Alexander Marshak[2], Dong L. Wu[2], Hongbin Yu[2,4], and Qiang Fu[5]

[1]Universities Space Research Association, Columbia, Maryland, USA, [2]NASA Goddard Space Flight Center, Greenbelt, Maryland, USA, [3]Science Systems and Applications Inc., Lanham, Maryland, USA, [4]Earth System Science Interdisciplinary Center, University of Maryland, College Park, Maryland, USA, [5]Department of Atmospheric Sciences, University of Washington, Seattle, Washington, USA

Abstract We present the first satellite-detected perturbations of the outgoing longwave radiation (OLR) associated with blowing snow events over the Antarctic ice sheet using data from Cloud-Aerosol Lidar with Orthogonal Polarization and Clouds and the Earth's Radiant Energy System. Significant cloud-free OLR differences are observed between the clear and blowing snow sky, with the sign and magnitude depending on season and time of the day. During nighttime, OLRs are usually larger when blowing snow is present; the average difference in OLRs between without and with blowing snow over the East Antarctic Ice Sheet is about $-5.2 \, W/m^2$ for the winter months of 2009. During daytime, in contrast, the OLR perturbation is usually smaller or even has the opposite sign. The observed seasonal variations and day-night differences in the OLR perturbation are consistent with theoretical calculations of the influence of blowing snow on OLR. Detailed atmospheric profiles are needed to quantify the radiative effect of blowing snow from the satellite observations.

1. Introduction

Blowing snow (BLSN), a common phenomenon over the polar regions, plays an important role in the studies of the Earth's cryosphere. It affects ice sheet mass balance and hydrological processes through redistributing surface mass and driving spatial and temporal variations in snow accumulation [e.g., *Palm et al.*, 2011; *Schmidt*, 1982]. BLSN can have a significant impact on the reconstruction of paleoclimate records by creating uncertainties in the inferred snow accumulation rate [*King et al.*, 2004]. The interaction between BLSN and light increases photon path length and affects the measurements of spaceborne lidar altimeters, such as the Advanced Topographic Laser Altimeter System (ATLAS) [e.g., *Yang et al.*, 2011].

The radiative effect of BLSN is multifold. In the shortwave region, BLSN depletes direct solar radiation reaching the surface, yet this depletion is largely compensated by the increase of diffuse solar flux [*Yamanouchi and Kawaguchi*, 1985]. Over the bright surface, the influence of BLSN on the outgoing solar radiation at the top of atmosphere (TOA) is small. In the longwave (LW) region, BLSN increases the downward LW flux and suppresses surface cooling by raising the emissivity of the atmospheric layer directly above the ground surface [e.g., *Lesins et al.*, 2009]. It is well known that a strong surface-based inversion (SBI) is a frequent feature over the Antarctic continent, especially over nighttime [e.g., *Zhang et al.*, 2011; *Hudson and Brandt*, 2005]. Studies have shown that SBIs still exist during BLSN events and mixing is usually limited to a very thin layer ($< 50 \, m$) above ground [*Mahesh et al.*, 2003; *Walden et al.*, 2003; *King*, 1990]. Part of the reason is that the persistent Antarctic wind is largely a result of the inversion; the presence of an inversion over the sloping terrain forces a wind through a local thermal wind mechanism [e.g., *Parish*, 1982]. Because of the existence of the strong SBI and the small water vapor amount in the Antarctic atmosphere, BLSN is expected to have a notable LW radiative effect at the TOA. Figure 1 illustrates this point with calculations using the Santa Barbara discrete ordinates radiative transfer Atmospheric Radiative Transfer model (SBDART) [*Ricchiazzi et al.*, 1998]. In these calculations, the conceptual atmosphere profiles (Figure 1a) for polar day and polar night are adapted from *Turner and Pendlebury* [2004] with boundary layer adjustment following the research of *Hudson and Brandt* [2005]. The profiles are based on the monthly mean at the Vostok Station (78.5°S 106.9°E) for January and July, respectively. For the polar night case, to represent wind-induced mixing, we allow a well-mixed 50 m layer above surface (inset of Figure 1a) [*Hudson*
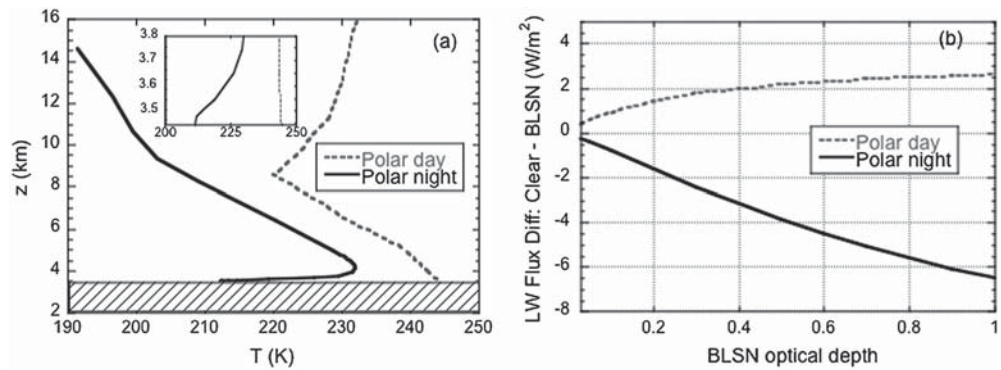
Figure 1. (a) Temperature profiles based on the Vostok Station (78.5°S 106.9°E) monthly mean for January (polar day) and July (polar night), respectively (data from *Turner and Pendlebury* [2004] and *Hudson and Brandt* [2005]); the inset shows the lower 400 m of the profiles. (b) TOA outgoing longwave flux differences between clear sky and blowing snow conditions as a function of optical depth for the temperature profiles given in Figure 1a. Calculations are done with the SBDART model. Blowing snow thickness assumed to be 0.2 km.

and Brandt, 2005; *King*, 1990]. In contrast to polar night, the SBI does not exist in the polar day profile, due to much stronger solar heating. The total column water vapor amount used in the calculation is 1 kg/m^2 for July and 2 kg/m^2 for January [*Johnsen et al.*, 2004]. The water vapor is vertically scaled to match the shape of the standard Arctic winter atmosphere, which is built in for SBDART. The TOA outgoing LW radiation (OLR) is integrated between 5 μm and 100 μm. A BLSN layer from the surface up to 200 m was inserted into the atmosphere profiles. The shape of BLSN particles is usually nearly spherical due to collisions and selective sublimation of the sharper convex corners [e.g., *Walden et al.*, 2003]. Here as a conceptual demonstration, BLSN is assumed to be spherical ice particles with an effective radius of 20 μm.

Figure 1b gives the modeling results of the BLSN LW radiative forcing at TOA, which is the difference of the outgoing LW fluxes (in this paper, TOA outgoing LW flux and OLR are used interchangeably) without and with BLSN. Let RF be the radiative forcing, then

$$RF = F^{\uparrow}_{clear} - F^{\uparrow}_{blsn} \qquad (1)$$

where $F^{\uparrow}_{clear}$ and $F^{\uparrow}_{blsn}$ are the TOA upward LW fluxes for cloud-free conditions without and with BLSN, respectively. Hence, a positive RF indicates that BLSN exerts a warming effect to the Earth-atmosphere system and vice versa. During polar night, because of the existence of the strong SBI (Figure 1a), a BLSN layer increases the TOA upward LW flux and results in a negative RF. In contrast, the same BLSN layer in the polar day gives rise to a positive RF because its temperature is cooler than that of the surface. For the given conceptual profiles, the LW radiative effect of a BLSN layer with an optical depth of 0.5 is about −3.9 and +2.2 Wm^{-2} for polar day and polar night, respectively.

Such a notable LW radiative effect by BLSN has not been corroborated by observations. Recently, *Palm et al.* [2011] developed a technique that enables BLSN detection, BLSN height, and optical depth retrieval on a global scale with observations from the Cloud-Aerosol Lidar with Orthogonal Polarization (CALIOP) on board the Cloud-Aerosol Lidar and Infrared Pathfinder Satellite Observations (CALIPSO) satellite [*Winker et al.*, 2009]. With this technique and by collocating CALIPSO and the Clouds and the Earth's Radiant Energy System (CERES) pixels, we are able to reclassify all the CERES pixels along the CALIPSO track into clear, cloudy, and BLSN categories. The reclassified data are then used in this study to investigate the changes in OLR associated with BLSN events as demonstrated in the case studies in section 2 and the statistical analysis in section 3.

2. Case Studies

To illustrate the synergetic approach used in this investigation, two case studies, one for a daytime BLSN event and the other nighttime, are presented. Data used for both cases include the Aqua Moderate Resolution Imaging Spectroradiometer (MODIS) Level 1b calibrated radiances, the CALIPSO Lidar Level 2 cloud layer product [*Winker et al.*, 2009], the *Palm et al.* [2011] BLSN detection results, and the Aqua CERES Single Scanner Satellite Footprint data [*Wielicki et al.*, 1996]. CALIPSO observations are near simultaneous with those from the MODIS and CERES instruments on Aqua (CALIPSO lags Aqua by less than 2 min) [*Winker et al.*, 2007]. For each case, we limit
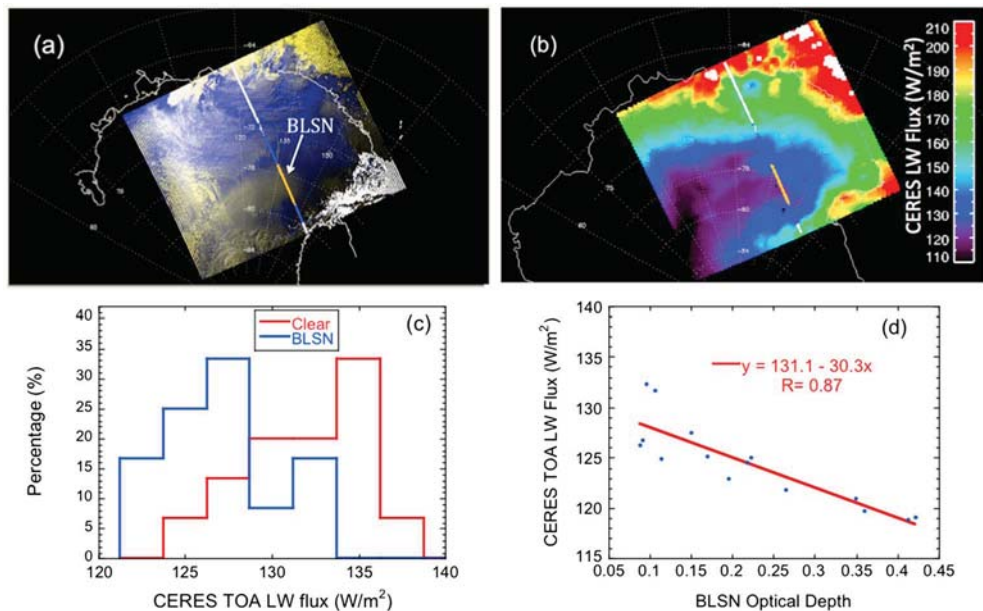
Figure 2. (a) Aqua MODIS false color image with 2.1 μm, 2.1 μm, and 0.85 μm as *R*, *G*, and *B* for 6 October 2009 at 07:00 UTC over East Antarctica. The thick line shows the CALIPSO track with each pixel classified as clear (blue), cloudy (white), and blowing snow (yellow). (b) The corresponding image from CERES of TOA LW flux overlaid with the corresponding CALIPSO track. (c) Distribution of LW flux for clear and blowing snow pixels along the CALIPSO track. (d) Relationship between CERE TOA LW flux and the optical depth of blowing snow pixels along the CALIPSO track.

our study area to a MODIS granule. The CERES pixels collocated with the corresponding CALIPSO track are extracted and reclassified into cloudy, clear, and BLSN, by combining the BLSN detection results with the CALIPSO operational products. Figure 2 shows the result for a daytime BLSN event on 6 October 2009 over East Antarctica. The reclassified CALIPSO pixels are displayed in blue (clear), white (cloudy), and yellow (BLSN) (CALIPSO track in Figures 2a and 2b). Overlaid with the CALIPSO track in Figure 2a is the corresponding Aqua MODIS false color image constructed with 2.1 μm, 2.1 μm, and 0.85 μm channels as *R*, *G*, and *B*. This combination makes BLSN stand out most prominently [*Palm et al.*, 2011]. For this case, the BLSN region shows up as a distinctive yellow color in the image. Figure 2b gives the corresponding Aqua CERES TOA upward LW flux image [*Loeb et al.*, 2005]. It is evident from Figures 2a and 2b that the BLSN region corresponds to smaller TOA upward LW fluxes compared to the nearby clear regions. Figure 2c shows the CERES outgoing LW flux distributions for clear and BLSN pixels along the CALIPSO track. Even though there exists an overlap between the two distributions, Figure 2c confirms that the OLRs of the clear pixels are generally larger than that of the BLSN pixels. Let F_{diff} be the difference between the mean values of the two categories, then

$$F_{\text{diff}} = \overline{F}^{\uparrow}_{\text{clear}} - \overline{F}^{\uparrow}_{\text{blsn}} \qquad (2)$$

where $\overline{F}^{\uparrow}_{\text{clear}}$ and $\overline{F}^{\uparrow}_{\text{blsn}}$ are the mean TOA upward LW fluxes for the CERES clear pixels and BLSN pixels, respectively. For this case, F_{diff} is 5.8 W/m^2, which is about 4.5% of the average clear sky LW flux. The positive sign of F_{diff} fits the expectation for an atmosphere profile without a SBI (Figure 1). The local time in the BLSN area for this case is around 4 P.M. The absence of a SBI is a reasonable assumption for this daytime case, when the surface warms much more than the air above it [*Hudson and Brandt*, 2005].

Here we distinguish F_{diff} with the BLSN LW radiative forcing RF (equation (1)). In addition to RF, other factors, such as potential differences in temperature profiles between clear and blowing snow scenes, uncertainties in CERES radiance-to-flux conversion, and uncertainties in scene classification, can also contribute to F_{diff}. At this stage, due to the lack of detailed atmospheric profile observations over the entire Antarctic ice sheet, it is not feasible to explicitly single out the LW radiative effects of blowing snow. However, as another evidence that blowing snow radiative effects is indeed a major contributing factor, Figure 2d shows that the observed TOA LW fluxes for BLSN pixels are highly correlated with BLSN layer optical depth (correlation coefficient = 0.87); similar correlation also exists between the LW fluxes and BLSN layer thickness (correlation
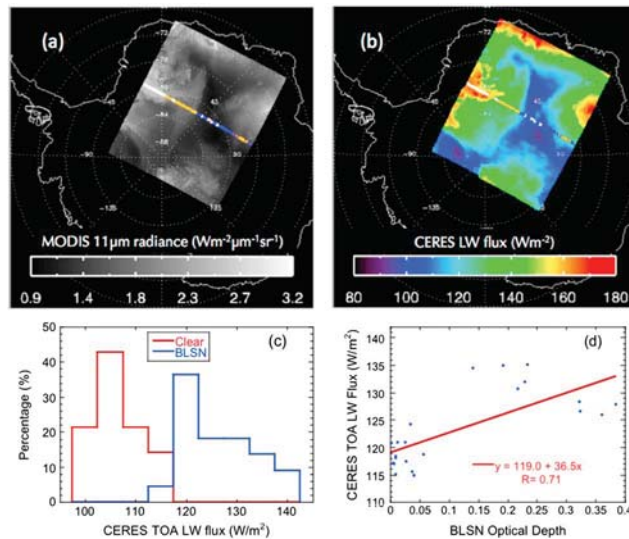
Figure 3. (a) Aqua MODIS 11 μm channel image for 2 August 2009 at 11:45 UTC over East Antarctica. The thick line shows the CALIPSO track with each pixel classified as clear (blue), cloudy (white), and blowing snow (yellow). (b) The corresponding image from CERES of TOA LW flux overlaid with the corresponding CALIPSO track. (c) Distribution of LW flux for clear and blowing snow pixels along the CALIPSO track. (d) Relationship between CERE TOA LW flux and the optical depth of blowing snow pixels along the CALIPSO track.

coefficient = 0.82; figure not shown), but no obvious correlation is observed between flux and surface elevation for this case (correlation coefficient = 0.01), which indicates that the contribution from geographical influences to the observed TOA LW flux differences is small.

Figure 3 gives the results of a nighttime BLSN case that took place on 2 August 2009 at 11:45 UTC over East Antarctica. The analysis procedure are generally the same as for the daytime case shown in Figure 2 except that the MODIS false color image given in Figure 2a cannot be constructed due to the lack of solar radiation. Instead, the MODIS 11 μm channel image is shown. As can be seen, the 11 μm radiances of the BLSN pixels (yellow) are higher than those of the clear pixels (blue), indicating a larger OLR with the presence of BLSN. This is confirmed by Figure 3b, which shows the corresponding CERES TOA LW fluxes. The distributions for clear and BLSN pixels along the CALIPSO track are given in Figure 3c. Compared to the 5.8 W/m^2 value for the daytime case, F_{diff} is −20.2 W/m^2 for this case. The negative value is expected because of the persistent SBIs over the Antarctica plateau during the polar night. Similar to the daytime case (Figure 2), the correlations are high between TOA LW fluxes and BLSN layer optical depth (correlation coefficient = 0.71; Figure 3d) and thickness (correlation coefficient = 0.83; figure not shown) but lower when it comes to surface elevation correlation coefficient = 0.19. These analyses show that even though we are unable to completely rule out the contributions from the geographical and meteorological influences, the results are consistent with the expectation of BLSN LW radiative effects.

3. Statistical Results

In order to investigate the spatial and temporal variability of F_{diff}, the CALIOP and collocated CERES observations for the whole year 2009 are analyzed. The A-train integrated CALIPSO, CloudSat, CERES, and MODIS merged product (C3M) [*Kato et al.*, 2010] is adopted for this study. The CERES pixels along the CALIPSO tracks are categorized into cloudy, clear, and BLSN classes. To limit the effect of environmental variability on the results, the Antarctic ice sheet is divided into grid boxes with a size of 2° latitude by 10° longitude. Then for each month, all the clear and BLSN CERES pixels are identified and put into their corresponding grid boxes. Then F_{diff} is calculated for each individual grid box following equation (2) if both the BLSN and the clear sky records exceed five in the box.

Figures 4a and 4b show the F_{diff} maps for January 2009 (Antarctic polar day) and August 2009 (Antarctic polar night). Figure 4c compares the distribution of the flux difference for January and August. Clearly, F_{diff} values for August are much more negative than that for January. While ~66% of the flux difference is positive in January, ~91% is negative in August. As discussed earlier, a negative F_{diff} means that the OLR under BLSN conditions are larger, indicating a cooling effect of BLSN to the Earth-atmosphere system. This occurs when
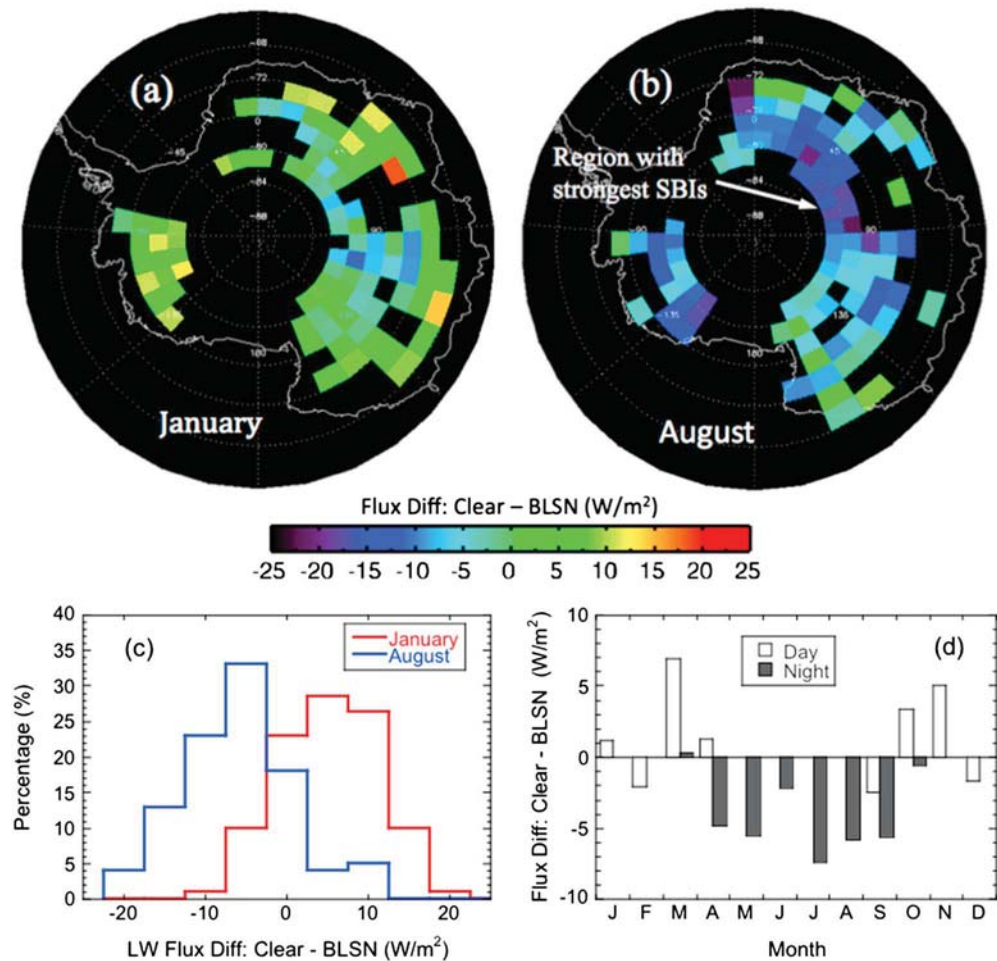
Figure 4. (a) CERES TOA LW flux differences between clear and blowing snow sky conditions over the Antarctic ice sheet for each 2° latitude by 10° longitude box for January 2009 (polar day). A positive value means the flux is larger for clear sky and vice versa; (b) same as Figure 4a but for August 2009 (polar night); (c) distributions of the data shown in Figures 4a and 4b; (d) differences between the monthly mean CERES TOA LW fluxes for clear and blowing snow sky conditions over East Antarctica for the year 2009.

SBIs are present (Figure 1). Previous studies [*Hudson and Brandt*, 2005; *Phillpot and Zillman*, 1970; *Zhang et al.*, 2011] have shown that the strength of SBIs anticorrelates with surface temperature. During the polar night (e.g., August), the intense LW radiative cooling at surface results in strong SBIs over Antarctica, especially in the interior of the plateau. Hence, everything else being equal, a BLSN event in August normally increases the OLR. The largest negative F_{diff} area in Figure 4b matches well with the region with the strongest SBIs [e.g., *Phillpot and Zillman*, 1970]. During January (polar day), due to the warming up of the surface, SBIs are destroyed over major parts of the ice sheet; hence, a BLSN layer can result in a positive F_{diff} (Figure 4a).

Not only do significant differences exist between the polar day months and the polar night months but also between daytime and nighttime within the same month (not shown). Strong LW radiative cooling establishes the SBIs during night, and solar heating may destroy them during the day [*Hudson and Brandt*, 2005]; hence, everything else being equal, the nighttime F_{diff} values are more negative compared to daytime.

Figure 4d presents the difference between the monthly mean CERES TOA LW fluxes for clear and BLSN sky conditions over the entire East Antarctic Ice Sheet (EAIS) for the year 2009. The EAIS lies between 45° West and 168° East longitudinally. We chose EAIS because of its relatively uniform surface feature and abundance of BLSN and clear sky observations. As clearly shown in the figure, during nighttime, when the SBIs are generally strong, the F_{diff} is mostly negative (7 out 8 months with data available), which is in good agreement with the expected BLSN LW radiative effect. The average F_{diff} is about $-5.2 \, W/m^2$ for the winter months (April to September) of 2009. During daytime, however, when SBIs are destroyed, F_{diff} values can become positive.

4. Conclusions

With BLSN detection results from the *Palm et al.* [2011] algorithm and data from CALIOP and CERES, this paper presents the first observational analysis of the OLR perturbation associated with BLSN events over the Antarctic ice sheet. We show that under cloud-free conditions, there exists significant difference between the OLRs with and without the presence of BLSN (F_{diff}). During nighttime, when the SBIs are generally strong, the OLR is larger when BLSN is present over most months (negative F_{diff}). The mean F_{diff} values over EAIS is about $-5.2\,\text{W/m}^2$ during the winter months of 2009. The strongest F_{diff} values occur over the region with the strongest SBIs. During daytime, when SBIs experience destructions, F_{diff} can be positive, which means that the OLR is smaller when BLSN is present. Climate in polar regions is sensitive to the radiative flux [*Bromwich et al.*, 2013]. The significant perturbations of LW radiation associated with BLSN events may affect climate in the regional and even global scale, which is currently not taken into account in climate models.

We emphasize again that in addition to the BLSN LW radiative effect, other factors may also contribute to the difference between clear and BLSN sky OLRs shown in this paper. These factors include meteorology, topography, uncertainties in CERES radiance-to-flux conversion and uncertainties in scene classification, etc. Due to the lack of detailed atmospheric profile observations over vast regions of the Antarctica ice sheet, it is not feasible to single out the BLSN LW radiative effect at this stage. However, this paper demonstrates that the major pattern of the observed differences between the OLRs with and without blowing snow matches the expectation of the LBSN LW radiative effects. More detailed Antarctica meteorological observations will be essential in pinpointing the BLSN LW radiative forcing.

References

Bromwich, D. H., F. O. Otieno, K. M. Hines, K. W. Manning, and E. Shilo (2013), Comprehensive evaluation of polar weather research and forecasting performance in the Antarctic, *J. Geophys. Res. Atmos.*, *118*, 274–292, doi:10.1029/2012JD018139.

Hudson, S. R., and R. E. Brandt (2005), A look at the surface-based temperature inversion over the Antarctic Plateau, *J. Clim.*, *18*, 1673–1696.

Johnsen, K.-P., J. Miao, and S. Q. Kidder (2004), Comparison of atmospheric water vapor over Antarctica derived from CHAMP/GPS and AMSU-B data, *Phys. Chem. Earth*, *29*, 251–255.

Kato, S., S. Sun-Mack, W. F. Miller, F. G. Rose, Y. Chen, P. Minnis, and B. A. Wielicki (2010), Relationships among cloud occurrence frequency, overlap, and effective thickness derived from CALIPSO and CloudSat merged cloud vertical profiles, *J. Geophys. Res.*, *115*, D00H28, doi:10.1029/2009JD012277.

King, J. C. (1990), Some measurements of turbulence over an Antarctic ice shelf, *Q. J. R. Meteorol. Soc.*, *116*, 379–400.

King, J. C., P. S. Anderson, D. G. Vaughan, G. W. Mann, and S. D. Mobbs (2004), Wind-borne redistribution of snow across an Antarctic ice rise, *J. Geophys. Res.*, *109*, D11104, doi:10.1029/2003JD004361.

Lesins, G., L. Bourdages, T. J. Duck, J. R. Drummond, E. W. Eloranta, and V. P. Walden (2009), Large surface radiative forcing from topographic blowing snow residuals measured in the High Arctic at Eureka, *Atmos. Chem. Phys.*, *9*, 1847–1862, doi:10.5194/acp-9-1847-2009.

Loeb, N. G., S. Kato, K. Loukachine, and N. Manalo-Smith (2005), Angular distribution models for top-of-atmosphere radiative flux estimation from the Clouds and the Earth's Radiant Energy System Instrument on the *Terra* satellite. Part I: Methodology, *J. Atmos. Oceanic Technol.*, *22*, 338–351.

Mahesh, A., R. Eager, J. R. Campbell, and J. D. Spinhirne (2003), Observations of blowing snow at the South Pole, *J. Geophys. Res.*, *108*(D22), 4707, doi:10.1029/2002JD003327.

Palm, S. P., Y. Yang, J. D. Spinhirne, and A. Marshak (2011), Satellite remote sensing of blowing snow properties over Antarctica, *J. Geophys. Res.*, *116*, D16123, doi:10.1029/2011JD015828.

Parish, T. R. (1982), Surface airflow over East Antarctica, *Mon. Weather Rev.*, *110*, 84–90.

Phillpot, H. R., and J. W. Zillman (1970), The surface temperature inversion over the Antarctic Continent, *J. Geophys. Res.*, *75*, 4161–4169.

Ricchiazzi, P., S. Yang, C. Gautier, and D. Sowle (1998), SBDART: A research and teaching software tool for plane-parallel radiative transfer in the Earth's atmosphere, *Bull. Am. Meteorol. Soc.*, *79*, 2101–2114.

Schmidt, R. A. (1982), Properties of blowing snow, *Rev. Geophys. Space Phys.*, *20*, 39–44.

Turner, J., and S. F. Pendlebury (Eds). (2004), *The International Antarctic Weather Forecasting Handbook*, xviii + 663 pp., British Antarctic Survey, Cambridge.

Walden, V. P., S. G. Warren, and E. Tuttle (2003), Atmospheric ice crystals over the Antarctic Plateau in winter, *J. Appl. Meteorol.*, *42*, 1391–1405.

Wielicki, B. A., B. R. Barkstrom, E. F. Harrison, R. B. Lee III, G. L. Smith, and J. E. Cooper (1996), Clouds and the Earth's Radiant Energy System (CERES): An Earth observing system experiment, *Bull. Am. Meteorol. Soc.*, *77*, 853–868.

Winker, D. M., W. H. Hunt, and M. J. McGill (2007), Initial performance assessment of CALIOP, *Geophys. Res. Lett.*, *34*, L19803, doi:10.1029/2007GL030135.

Winker, D. M., M. A. Vaughan, A. Omar, Y. Hu, K. A. Powell, Z. Liu, W. H. Hunt, and S. A. Young (2009), Overview of the CALIPSO mission and CALIOP data processing algorithms, *J. Atmos. Oceanic Technol.*, *26*, 2310–2323.

Yamanouchi, T., and S. Kawaguchi (1985), Effects of drifting snow on surface radiation budget in the katabatic wind zone, Antarctica, *Ann. Glaciol.*, *6*, 238–241.

Yang, Y., A. Marshak, S. P. Palm, T. Varnai, and W. J. Wiscombe (2011), Cloud impact on surface altimetry from a 532 nm space-borne micro-pulse photon counting lidar-Part I: System modeling for cloudy and clear atmospheres, *IEEE Trans. Geosci. Remote Sens.*, *49*, 4910–4919.

Zhang, Y., D. J. Seidel, J.-C. Golaz, C. Deser, and R. Tomas (2011), Climatological characteristics of Arctic and Antarctic surface-based inversions, *J. Clim.*, *24*, 5167–5186.